Evolving Bifacial Molecule Strategy for Surface Passivation of Lead Halide Perovskite Solar Cells

Journal:	*Sustainable Energy & Fuels*
Manuscript ID	SE-ART-08-2024-001096
Article Type:	Paper
Date Submitted by the Author:	10-Aug-2024
Complete List of Authors:	Minoi, Nanaki; Osaka University, Department of Applied Chemistry, Graduate School of Engineering Ishiwari, Fumitaka; Osaka University, Graduate School of Engineering Omine, Takuya; Osaka University, Graduate School of Engineering Murotani, Kazuharu; Osaka University, Department of Applied Chemistry, Graduate School of Engineering Nishikubo, Ryosuke; Osaka University, Department of Applied Chemistry Saeki, Akinori; Osaka University, Department of Applied Chemistry, Graduate School of Engineering

SCHOLARONE™
Manuscripts

ARTICLE

Evolving Bifacial Molecule Strategy for Surface Passivation of Lead Halide Perovskite Solar Cells†

Nanaki Minoi,[a] Fumitaka Ishiwari,[a,b,c*] Takuya Omine,[a] Kazuharu Murotani,[a] Ryosuke Nishikubo[a,b] and Akinori Saeki[a,b*]

A variety of passivation molecules have enhanced the performance and stability of organic–inorganic lead halide perovskite solar cell (PSCs); however, the tailoring of the design of these molecules remains largely unexplored. In this work, we propose two new classes of passivation molecules: a C_2-symmetric *syn*-type bifacial donor–π–donor molecule and a C_3-symmetric *syn*-type bifacial truxene. The former (PM-*syn*) bears hydrophobic alkylphenyls and hydrophilic diethylene glycol-substituted phenyls on each face of the indenofluorene π-core. Owing to the efficient hole transfer and surface passivation by the flanked donor units, PM-*syn* (a racemate of enantiomers) exhibited an improved power conversion efficiency (PCE) of 18.79% and long-term stability compared with the control device (17.98%). The latter, bifacial truxene (TRX-*syn*), appended with three carboxyl units on one face, exhibited an improved PCE (19.76%) and stability, demonstrating the general effectiveness of the bifacial molecular concept in the passivation of PSC. Comparative spectroscopic and time-resolved studies of bifacial molecules and their *anti*-type analogues support our claims and provide a rich area for the design of new molecules for the modification of perovskite layers.

Introduction

An organic-inorganic lead halide perovskite solar cell (PSC) is a highly beneficial technology that is promising for light energy harvesting at low cost and with high efficiency.[1–3] Perovskite (PVK) is a crystal structure with an ABX_3 composition composed of organic cations (A), metal cations (B), and halogen anions (X).[4–6] They offer a high power conversion efficiency (PCE) owing to their exceptional optoelectronic properties, such as a high absorption coefficient ($>10^5$ cm^{-1}) based on direct transitions,[7] low exciton binding energy (~20 meV) allowing free charge carrier generation at room temperature,[8] bi-polar charge transport properties,[9] and large diffusion lengths (1–100 μm) and mobilities.[10,11] Continuously updated PCE records currently exceed 26%, being close to that of inorganic silicon solar cells.[12,13]

Despite the numerous advantages of PSCs, significant challenges remain regarding their practical applications. While enhancing the PCE, the primary obstacle facing them is the stability of the PSCs, which are prone to degrade when exposed to atmospheric moisture, heat, and light.[14,15] Various approaches to addressing these issues have been explored, including modifying the PVK crystal composition, introducing additives that promote PVK crystal growth,[16,17] and developing new electron transport layers (ETL) and hole transport layers (HTL).[18,19] Although PVK crystals are relatively defect-tolerant semiconductors,[20] numerous defects exist at the PVK layer interfaces with ETL or HTL, and recent attention has focused on developing new methods to passivate those defects.[21] The defects are known to adversely affect efficiency through trap-assisted recombination[22] and diminished durability due to the formation of degradation centers.[23]

To mitigate these defects, many passivation agents have been examined, including ammonium salts,[24] zwitterions,[25] alkali metal salts,[26] Lewis bases small molecules,[27] and polymers.[28] Particularly, the development of passivation molecules (PMs), which inherently possess multifunctional properties for PVK passivation, has been actively investigated.[29] PM design often incorporates cyano groups,[30] carbonyl groups,[31] and phosphine oxides[32] that may coordinate with PVK surface defects. The backbone structures of D−A−D (donor-acceptor-donor)[33] and A−D−A (acceptor-donor-acceptor)[34] enable us to tune their energy levels such that they are suitable for the PVK/HTL (or ETL) interface. Furthermore, the dipole moment of a molecule is interesting, as it can modulate band bending for improved charge extraction.[35] Because of its synthetic accessibility and simple design, these PMs are symmetrical in their longitudinal and perpendicular directions. In contrast, we have recently proposed an asymmetric, bifacial molecular concept as a novel PM design that consists of indeno-[1,2-*b*]fluorene (IDF) π-core and flanked triphenylamine (TPA)

[a.] Department of Applied Chemistry, Graduate School of Engineering, Osaka University, 2-1 Yamadaoka, Suita, Osaka 565-0871, Japan

[b.] Innovative Catalysis Science Division, Institute for Open and Transdisciplinary Research Initiatives (ICS-OTRI), Osaka University, 1-1 Yamadaoka, Suita, Osaka 565-0871, Japan.

[c.] PRESTO, Japan Science and Technology Agency (JST), Kawaguchi, Saitama 332-0012, Japan.
E-mail: ishiwari@chem.eng.osaka-u.ac.jp (F.I.); saeki@chem.eng.osaka-u.ac.jp (A.S.)
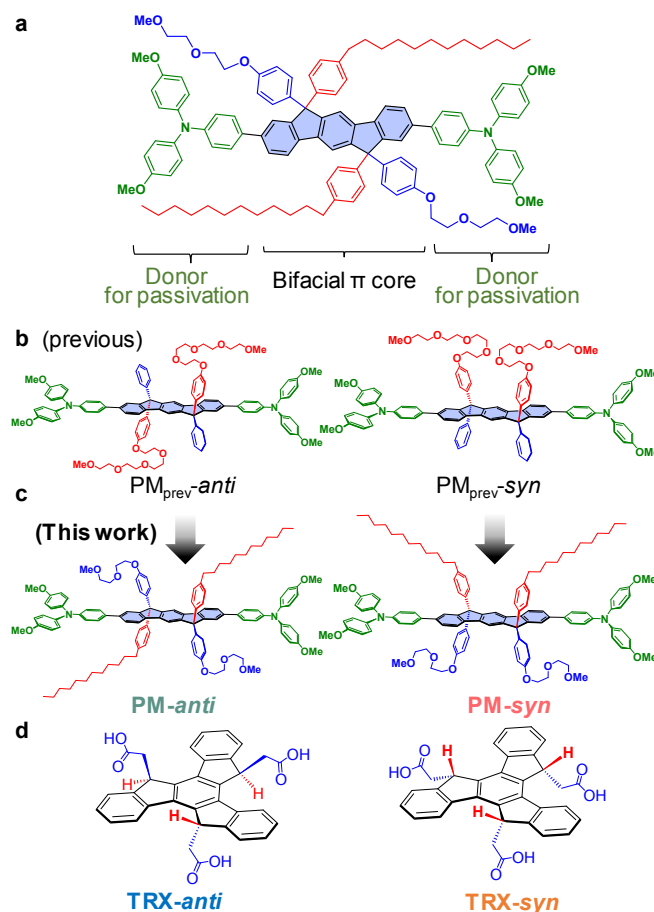
Fig 1. (a) Molecular structure of D−π−D PM examined in this study. (b) Previous PM structures (PM$_{prev}$-*anti* and PM$_{prev}$-*syn*)[36] and (c) new PM structures (PM-*anti* and PM-*anti*) in this work. (d) Molecular structures of TRX-anti and TRX-syn. Note that the structure of only single enantiomers is shown for the *syn*-type molecules (a racemic mixture in the experiments).

donor units (**Fig. 1a**).[36] The lone pair of nitrogen of TPA is assumed to passivate the undercoordinated Pb^{2+}.[37] As shown in **Fig. 1b**, the IDF unit yields *anti-* and *syn*-(racemic) isomers, which provide two types of geometries having hydrophilic tetraethylene glycol (TEG) and hydrophobic phenyl units in the opposite side and the same side, respectively. This *syn*-type D−π−D PM in our previous work (PM$_{prev}$-*syn*) exhibited excellent hole transfer from PVK owing to their energy level-matched highest occupied molecular orbital (HOMO), good wettability with PVK layer, and modification of PVK surface (a partial removal of remnant PbI$_2$ and change of crystallite orientation of PVK). These effects were less pronounced for the *anti*-type PM (PM$_{prev}$-*anti*). The PSC passivated with PM$_{prev}$-*syn* showed a maximum PCE of 19.74%, which was higher than that of the PM$_{prev}$-*anti* passivation (19.49%) and the control without passivation (18.43%). Another example of a bifacial PMs is a triptycene molecule appended with three alkylamines on one side in the vertical direction.[38] Despite the absence of reference isomers in this case, the 1,8,13-tris (ammoniomethyl)triptycene triiodide [(TAMT)I$_3$] molecule showed improved PCE by surface passivation.

In this study, we evolved a bifacial molecular design of D−π−D PM for passivating PSCs by tuning its hydrophilic and hydrophobic chains and examined the generality of bifacial molecular strategy by introducing another C_3-symmetric molecule. The chemical structure of the former is shown in **Fig. 1c**. PM-*anti* has hydrophobic *n*-dodecylphenyl chains and hydrophilic diethylene glycol (DEG)-phenyl units at the *anti* position, whereas PM-*syn* (racemic) has these units on each face at the *syn* position. Compared to the previous D−π−D PM, its hydrophobic phenyl unit was replaced by alkylphenyl to increase hydrophobicity and thus prevent the penetration of water, because the previous PM did not show a noticeable improvement in stability despite the increase of initial PCE value.[37] In addition, the hydrophilic TEG-phenyl unit of the previous D−π−D PM was replaced by DEG-phenyl to reduce the steric hindrance and facilitate a better coordination to a PVK layer.

As a bifacial C_3-symmetric motif, we designed new tricarboxyl truxene (TRX) molecules.[39,40] As shown in **Fig. 1d**, they have *anti-* and *syn*-isomers, namely TRX-*anti* and TRX-*syn* (a racemic mixture), where the carboxylates are expected to passivate PVK via the same mechanism as TPA.[37,41] There are a few reports on the use of TRX derivatives in PSCs: one is TRX appended with TPA, which is utilised as an HTL[42] or passivator of NiOx.[43] The other is TRX appended with pyridine for the passivation of the PVK layer.[44] In both cases, the TRX unit is functionalized at its three peripheral benzene rings and solubilised using six alkyl chains at the 5, 10, and 15 positions (at the place of H and COOH units in **Fig. 1d**). Phosphonic acid-functionalized triazatruxene (TAT) is also another example of C_3-symmetric molecule that is used as the functionalization of transparent conductive oxide (TCO) as a hole-collecting monolayer.[45] These TRXs and TAT constitute a symmetric π-plane, whereas our TRX is a simple, bifacial motif, which may enable a balanced functionalization of passivation on the bottom, prevention of water penetration on the top, and efficient hole transfer through the face-on π-plane.

Results and Discussion

We synthesised PM-*anti*, PM-*syn*, TRX-*anti*, and TRX-*syn* according to previous reports.[36,40] Briefly, PMs and TRXs were synthesised in six and three steps, respectively, from commercially available compounds[36,40] (See the ESI for details). These molecules were characterised by ^{1}H NMR, ^{13}C NMR, high-resolution fast atom bombardment (FAB) mass spectrometry, Fourier transform infrared (FT-IR) spectrometry, and analytical high-pressure liquid chromatography (HPLC), as shown in **Figs. S1–S20(ESI†)**. Silica gel chromatography allowed the separation of the *anti-* and *syn*-isomers of both PM and TRX. The chiral PM-*syn* and achiral PM-*anti* molecules were confirmed using chiral HPLC with circular dichroism as shown in **Fig. S20(ESI†)**.

Figure 2a shows the ultraviolet-visible (UV-vis) absorption spectra of PM-*anti* and PM-*syn* in chloroform. They are almost identical in terms of their shapes and peak intensities (molar extinction coefficient, ε of 7.6×10^4 dm^3 mol^{-1} cm^{-1} at 394 nm), consistent with the previous PM$_{prev}$-*anti* and PM$_{prev}$-*syn* having

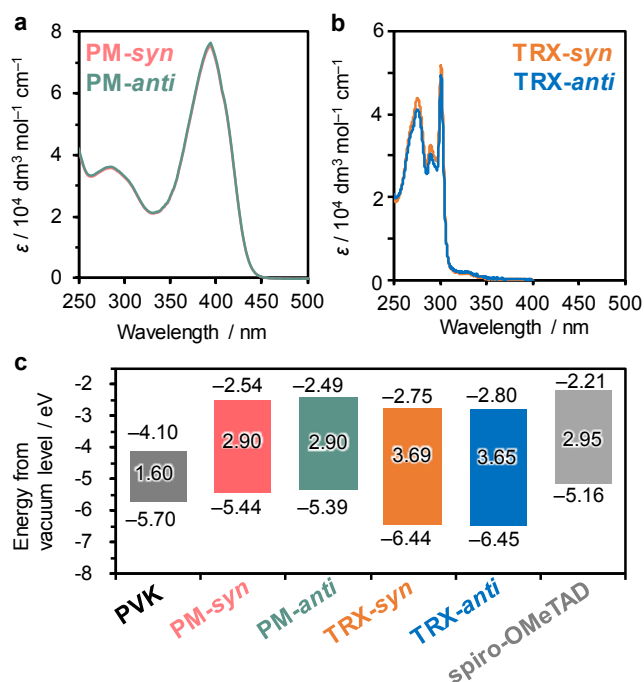**Fig 2.** (a) UV-vis absorption spectra of PM-*syn* and PM-*anti* in chloroform (5 µmol dm⁻³). (b) UV-vis absorption spectra of TRX-*syn* and TRX-*anti* in THF (15 µmol dm⁻³). (c) Energy diagram of PVK (MA$_{0.13}$FA$_{0.87}$PbI$_{2.61}$Br$_{0.39}$),[36] PMs, TRXs, and spiro-OMeTAD[36] evaluated by PYS (HOMO) and optical bandgap (**Fig. S22(ESI†)**).

the same backbone with different side chains (ε of 7.2 × 10⁴ dm³ mol⁻¹ cm⁻¹ at 394 nm).[36] We assume that these molecules are D–π–D rather than D–A–D, because the lowest unoccupied molecular orbital (LUMO) calculated by density functional theory (DFT) is extended to the peripheral benzene of flanked donor TPA, and HOMO is spread over the entire backbone (**Fig. S21(ESI†)**). This is supported by the UV-vis absorption spectra of the building blocks, which indicate the primary contribution of methoxy-substituted TPA to those of PM$_{prev}$-*anti* and PM$_{prev}$-*syn*.[36] As shown in **Fig. 2b**, TRX-*anti* and TRX-*syn* also exhibit the same photoabsorption spectra in tetrahydrofuran (THF), while their ε values at the peak of 301 nm deviate slightly from each other (4.9 × 10⁴ and 5.2 × 10⁴ dm³ mol⁻¹ cm⁻¹, respectively). Interestingly, the TRX molecules comprise weak photoabsorption in 320–350 nm, which is ascribed to the symmetry-forbidden lowest-energy transition[46] and is key to the chiroptical properties once they are resolved into enantiopure compounds.[40] The HOMO energy levels of the molecules were measured by photoelectron yield spectroscopy (PYS), and bandgap energies (E_g) were calculated from the absorption edge (data are provided in **Fig. S22(ESI†)**). All PM and TRX molecules are transparent in the visible-light region (the optical bandgap, E_g are 2.90 and 3.65–3.69 eV, respectively), corroborating the absence of light filtering effect on PSCs. The resultant energy level diagram including LUMO (= HOMO + E_g) is displayed in **Fig. 2c**. The HOMO energy levels of PM-*anti* (−5.39 eV) and PM-*syn* (−5.44 eV) are located in between −5.70 eV of the valence band maximum (VBM) of the mix-cation/mix-halide Pb-PVK (MA$_{0.13}$FA$_{0.87}$PbI$_{2.61}$Br$_{0.39}$, where

MA is methylammonium and FA is formamidinium)[47,48] and −5.16 eV of the HOMO energy level of spiro-OMeTAD HTL, which allows for a hole transfer from PVK to PM and HTL owing to their cascade energy alignment. In sharp contrast, the HOMO energy levels of TRX-*anti* (−6.45 eV) and TRX-*syn* (−6.44 eV) are deeper than the VBM of PVK, which needs a TRX layer as thin as possible to extract holes from the PVK layer. Both the PM and TRX molecules inherently possess hole-blocking abilities because their LUMO energy levels are far shallower than the conduction band minimum (CBM) of PVK.

The shallow HOMO energy levels of PM and the deep ones of TRX led to contrasting changes in the photoluminescence (PL) spectra of PVK. The PL intensity of PVK with a thin PM-*anti* deposition (PVK/PM-*anti*) exhibited a dramatic quenching of 14% relative to that of PVK treated with CB (PVK/CB, **Fig. 3a**). Moreover, the deposition of PM-*syn* (PVK/PM-*syn*) promoted quenching to 7%. Quenching is readily explained by hole transfer from PVK to PMs. In addition to the quenching, the coordination of PM on Pb²⁺ has been confirmed by X-ray photoelectron spectroscopy (XPS).[36] On the contrary, TRX-*anti* showed mostly unchanged PL intensity (94%), while TRX-*syn* showed increased PL (111%). The increased PL is in accordance with the observations in typical passivation molecules, which is understood from the defect passivation and resultant increase in radiative decays.[21,37]

The hole transfer from PVK to PM-*anti* or PM-*syn* was investigated in detail using time-resolved photoluminescence (TRPL). As shown in **Fig. 3c**, the averaged lifetime (τ_{ave}) of PVK/PM-*anti* (167 ns) is much shorter than the reference of PVK/CB (1099 ns, **Table S1(ESI†)**). The τ_{ave} of PVK/PM-*syn* was
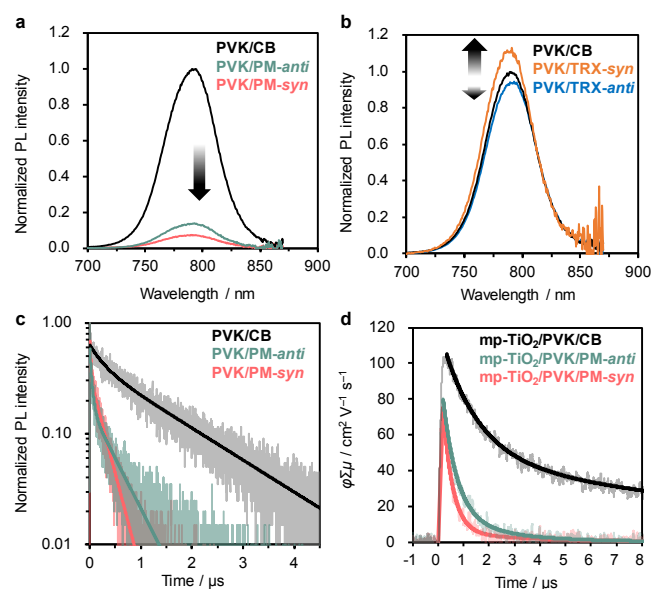

Fig 3. PL spectra of (a) PVK with/without PM-*syn* or PM-*anti* passivation and (b) PVK with/without TRX-*syn* or TRX-*anti* passivation (λ_{ex} = 500 nm). The noise at > 850 nm is caused by sensitivity calibration. (c) TRPL decays of PVK w/without PM-*syn* or PM-*anti* passivation (λ_{ex} = 377 nm, λ_{em} = 770 nm). (e) TRMC decays of PVK on mp-TiO₂ with/without PM-*syn* or PM-*anti* passivation (λ_{ex} = 500 nm). The solid thick lines in (c) and (d) are double exponential fitting curves.

further shortened to 128 ns, which was in good agreement with the steady-state PL measurements. The hole transfer dynamics from PVK to PMs were evaluated more directly than TRPL by using flash-photolysis time-resolved microwave conductivity (TRMC).[49–51] As shown in **Fig. 3d**, PVK prepared on mesoporous TiO$_2$ (mp-TiO$_2$) exhibits a long decay (τ_{ave} = 7.72 µs, **Table S2(ESI†)**) which can be attributed to surviving holes in the PVK layer, since the photogenerated electrons are immediately captured by the underlying mp-TiO$_2$ ETL.[11] The deposition of PM-*anti* (mp-TiO$_2$/PVK/PM-*anti*) exhibited an accelerated decay with τ_{ave} = 0.88 µs, and notably, the deposition of PM-*syn* (mp-TiO$_2$/PVK/PM-*syn*) showed the shortest τ_{ave} of 0.59 µs. These TRMC results are consistent with the TRPL and PL results. Although the quenching in PL, TRPL, and TRMC is significant, the hole transfer to HTL (doped spiro-OMeTAD) is efficient as confirmed previously in PVK/passivation/HTL samples.[36] We also examined other concentrations of the PM solution (1, 3, and 5 mg mL^{-1}) and found small deviations in their PL quenching (**Fig. S23(ESI†)**), TRPL lifetimes (**Fig. S24(ESI†)**), and TRMC decays (**Fig. S25(ESI†)**). However, the sample processed with a 3-mg mL^{-1} solution showed the shortest τ_{ave} of TRPL and TRMC. From **Fig. 3d**, most of the holes are quenched within ~4 µs, which is fast enough to extract holes in the PSC devices.[52] Note that the hole transfer process of PMs is more efficient than that of previous PMs (PL > 65%, TRPL τ_{ave} > 479 ns, TRMC τ_{ave} > 0.96 µs, **Tables S1 and S2(ESI†)**).[36] In contrast to PM-*syn* and PM-*anti* that have a hole transfer capability, treatment with TRX-*syn* and TRX-*anti* showed no acceleration in TRPL and TRMC decays (**Fig. S26 (ESI†)**). Notably, PVK on TRX-*syn* exhibits the longest τ_{ave} of TRPL (1.20 µs) and TRMC (12.1 µs), being consistent with the increased PL intensity (**Fig. 3b**) and indicating its most efficient passivation (**Tables S1 and S2 (ESI†)**).

To evaluate the hydrophobicity of the PMs- and TRX-coated PVK layers, we measured the contact angle (CA) of these films and displayed snapshots along with the CA values in **Fig. 4**. PM-*anti* and PM-*syn*-processed PVKs showed the CA values of 93.1 ± 5.1° and 93.5 ± 4.0°, respectively, indicating the improved hydrophobicity compared to the PVK layer (66.8 ± 1.7°) (**Fig. 4a**).

This is in sharp contrast to the previous PM$_{prev}$-*syn* that showed increased hydrophilicity (CA = 58.6 ± 2.0°).[36] Indeed this result is in accordance with our expectation for the new PM-*syn*, because its hydrophobic part is enriched (phenyl is replaced by *n*-dodecylphenyl), and its hydrophilic part is depleted (TEG is replaced by DEG). Although PM$_{prev}$-*anti* exhibited a hydrophobic nature (CA = 76.1 ± 1.3°), there were no notable differences between the present PM-*anti* and PM-*syn*. This is probably because the long alkyl chains (*n*-dodecylphenyl) of the PMs dominated the polarity of the thin films. On the other hand, there was no notable change in the CA values of the TRX-modified PVKs, PVK/IPA: 77.0 ± 2.9°, PVK/TRX-*syn*: 70.8 ± 12.6°, and PVK/TRX-*anti*: 76.8 ± 1.6° (**Fig. 4b**). This may be linked to the lower concentration of TRX solutions (0.5 mg mL^{-1} in IPA) than those of PMs (3 mg mL^{-1} in CB) because TRXs are less soluble than PMs. In particular, TRX-*anti* showed over 100 nm agglomeration as observed in dynamic light scattering (DLS) measurements (**Fig. S27(ESI†)**). Note that such a large agglomeration was not observed in scanning electron microscopy (SEM) images of TRX-*anti*-treated perovskite (**Fig. S28(ESI†)**), consistent with the large particle-sensitive DLS.

The effect of passivation on the perovskite surface crystallites was examined using 2-dimensional grazing-
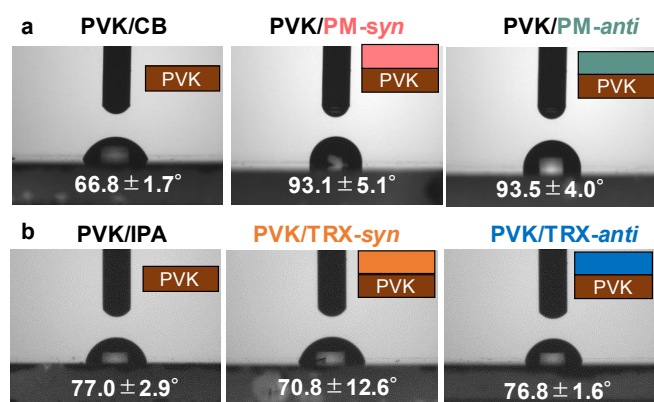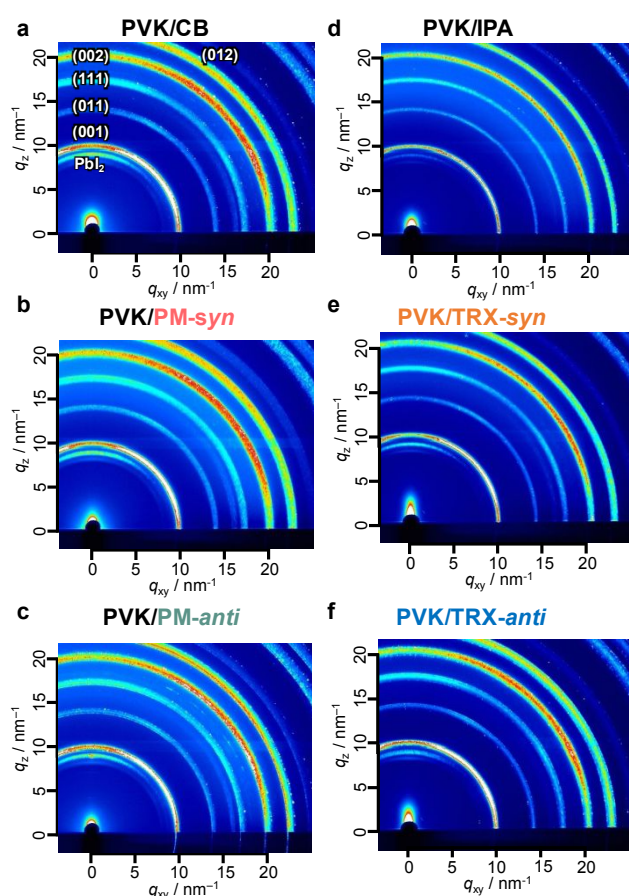

Fig 4. Images of contact angle measurements (water droplet) of (a) PVK with/without PM-*syn* or PM-*anti* passivation and (b) PVK with/without TRX-*syn* or TRX-*anti* passivation.

Fig 5. 2D-GIXRD images of (a)-(c) PVK with/without PM-*syn* and PM-*anti* passivation and (d)-(f) PVK with/without TRX-*syn* and TRX-*anti* passivation. The crystal indices of cubic phase (α-phase) of PAPbI$_3$ are appended in (a).

Table 1. Summary of PSC devices with/without passivation.[a]

Passivation	PCE / %	J_{SC} / mA cm^{-2}	V_{OC} / V	FF	HI[b]	Device No.
Control	15.99 ± 0.60 (17.98)	24.18 ± 0.56 (24.87)	0.977 ± 0.007 (0.988)	0.676 ± 0.016 (0.732)	0.15 ± 0.07 (0.10)	6
PM-*syn*[c]	16.85 ± 0.34 (18.79)	24.20 ± 0.52 (24.84)	0.990 ± 0.007 (1.013)	0.703 ± 0.010 (0.747)	0.11 ± 0.04 (0.07)	6
PM-*anti*[c]	17.01 ± 0.39 (18.71)	24.41 ± 0.38 (24.92)	0.985 ± 0.012 (1.008)	0.707 ± 0.004 (0.745)	0.08 ± 0.04 (0.11)	6
TRX-*syn*[d]	18.09 ± 0.43 (19.76)	24.79 ± 0.42 (25.47)	1.038 ± 0.006 (1.051)	0.703 ± 0.007 (0.738)	0.09 ± 0.04 (0.10)	6
TRX-*anti*[d]	16.66 ± 0.57 (18.70)	24.83 ± 0.42 (25.32)	0.997 ± 0.007 (1.011)	0.672 ± 0.016 (0.731)	0.19 ± 0.06 (0.17)	8

[a] FTO/mpTiO$_2$/MA$_{0.13}$FA$_{0.87}$PbI$_{2.61}$Br$_{0.39}$/passivation/spiro-OMeTAD(doped)/Au under 1 sun (100 mW cm^{-2}). Values in parentheses are the maximum values. The average values were calculated for forward and reverse scans in multiple devices. The error values are the standard deviations of multiple devices for the forward and reverse scans. [b] Hysteresis index (HI) = (reverse PCE − forward PCE)/(reverse PCE). [c] Processed from a 3-mg mL^{-1} CB solution. [d] Processed from a 0.5-mg mL^{-1} IPA solution.

incidence X-ray diffraction (2D-GIXRD). As shown in **Fig. 5**, all the samples yield arc-shaped diffractions at the scattering vectors (*q*) of ~10, 14, 17, 20, and 22 nm^{-1}, readily attributed to (001), (011), (111), (002), and (012) of cubic phase (α-phase) of PAPbI$_3$ (the out-of-plane and in-plane profiles are provided in **Fig. S29(ESI†)**).[53] In addition, one sharp peak due to remaining PbI$_2$ is observed at *q* ~ 9 nm^{-1} in the out-of-plane direction, because we added excess PbI$_2$ to the precursor (FAI/PbI$_2$ = 0.95), which has a positive impact on the PSC performance.[54] The peak of PbI$_2$ in powder X-ray diffraction in the out-of-plane is more distinct than those of 2D-GIXRD, confirming the presence of PbI$_2$ on the surface (**Fig. S30(ESI†)**). After passivation, no apparent changes were observed in the PM-*syn* and PM-*anti*-treated PVKs (**Figs. 5b–5c**) or TRX-*syn* and TRX-*anti*-treated PVKs (**Figs. 5e–5f**). This result differs from the previous PM$_{prev}$-*syn* that exhibited a removal of remnant PbI$_2$ and a change in the orientation of the perovskite crystallites on the surface.[36] We assumed that PM$_{prev}$-*syn*-bearing TEG units on the same face effectively coordinated Pb^{2+} in a chelating-like manner and dissolved remnant PbI$_2$ during the passivation process. A similar removal of remnant PbI$_2$ on the surface has been reported by

using passivation or washing agents such as phenethylammonium iodide,[55] benzylamine hydroiodide[56] and (*S*)−3-Amino-4-phenylbutyric acid hydrochloride.[57] However, the present PM-*syn* has shorter DEG units, which may be unable to chelate Pb^{2+}. This is also supported by SEM images that show the presence of PbI$_2$ crystals (a long shape with a less conductive bright colour) on the surface, even after passivation treatment (**Fig. S31(ESI†)**). We also performed 2D-GIXRD measurements on the pristine films of the PMs and TRXs and found no peaks other than broad halos (**Fig. S32(ESI†)**). Stemming from this amorphous nature, PM-*syn* and PM-*anti* exhibited one order of magnitude smaller space-charge-limited current (SCLC) mobilities of holes (μ_h = 4.8 × 10^{-6} and 9.9 × 10^{-6} cm^2 V^{-1} s^{-1}, respectively) than those of spiro-OMeTAD (5.1 × 10^{-5} cm^2 V^{-1} s^{-1}, **Fig. S33** and **Table S3(ESI†)**). The μ_h of PM-*syn* and PM-*anti* are smaller than those of 1.5 × 10^{-4} cm^2 V^{-1} s^{-1} for PM$_{prev}$-*syn* and
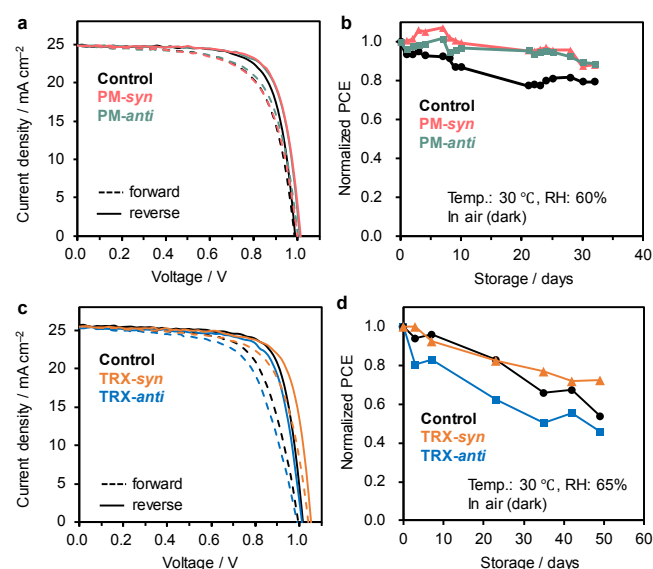

Fig 6. (a) Best-performing *J–V* curves of PSCs with/without PM-*syn* or PM-*anti* passivation. (b) Normalised PCE during storage. Temperature: 30 °C and RH: 60% in the air and darkness. (c) Best-performing *J–V* curves of PSCs with/without TRX-*syn* or TRX-*anti* passivation. (d) Normalized PCE during storage. Temperature: 30 °C and RH: 65% in the air and darkness.

5.4×10^{-5} cm^2 V^{-1} s^{-1} PM$_{prev}$-*anti*,[36] which could be due to the insulating long alkyl chains of the present PMs.

Figure 6a shows the current density (*J*)–voltage (*J–V*) curves of the best PSC devices that adopted the normal device structure of fluorine-doped tin oxide (FTO)/compact TiO$_2$/mpTiO$_2$/PVK (w/wo PM)/doped spiro-OMeTAD/Au. Passivation via PM-*syn* and PM-*anti* realised an improved PCE of 18.79 and 18.71%, respectively, compared with the control device (17.98%) (**Table 1**). The increase in PCE is mainly caused by an open-circuit voltage (*V*$_{OC}$) of 1.008–1.013 V (control: 0.988 V) and fill factor (FF) of 0.745–0.747 (control: 0.732), while the short-circuit current density (*J*$_{SC}$) values are comparable (~24.8–24.9 mA cm^{-2}). External quantum efficiency (EQE) spectra are presented in **Fig. S34(ESI†)**, and the *J–V* curves of different concentrations of PMs in CB (1, 3, and 5 mg mL^{-1}) and their EQE spectra are appended in **Figs. S35** and **S36(ESI†)** (the values are listed in **Table S4(ESI†)**). The optimal concentration of PM-*syn* and PM-*anti* was 3 mg mL^{-1}, which is the same as that of the previous PM and is consistent with the fastest hole transfer rates observed in TRPL and TRMC. Notably, the PSCs treated with PM-*syn* and PM-*anti* without encapsulation showed good stability during storage (32 days) in air and darkness, preserving ~90% of the initial PCE values, which was clearly an improvement over the control device, showing a decrease in PCE to ~80% (**Fig. 6b**). The stability is an improvement over the previous PMs that show the high initial PCE values but almost similar degradation among the control and PM-passivated PSCs.[36] The better stability of the PM-*syn* and PM-*anti*-treated PSCs than the previous ones can presumably be ascribed to the higher hydrophobicity of the former, as evidenced by the CA measurements, underpinning the effectiveness of bifacial molecular design that simultaneously facilitates defect passivation, hole transfer, and water blocking.

Interestingly, we observed contrasting initial PCE values between the TRX-*syn* and TRX-*anti*-treated PSCs, as shown by the *J–V* curves (**Fig. 6c**) and listed in **Table 1**. The former was 19.76%, whereas the latter was 18.70%, mostly because of the increased *V*$_{OC}$ values upon passivation (1.051 vs. 1.011 V). Thus, we are claiming the generality of the bifacial molecular design for the passivation of PSCs. Moreover, the TRX-*syn*-treated PSC maintained a PCE of ~73% after 50 days of storage in air, which was better than that of the control (~54%) and TRX-*anti*-treated PSCs (~46%) (**Fig. 6d**). The hydrophobic π-plane of TRX on the PVK surface may contribute to the improved stability, although a distinguishable change in CA was not observed. Associated with the deep HOMO energy levels of TRXs, the optimal concentration for TRX passivation was as low as 0.5 mg mL^{-1}. The *J–V* curves and EQE spectra at different TRX concentrations are shown in **Figs. S37** and **S38(ESI†)**. In summary, we revealed the general effectiveness of a bifacial strategy in D–π–D and TRX passivation molecules that have hydrophobic and hydrophilic parts on each face of the π-plane. Despite these molecules have different π planes, it is interesting to find a general, positive impact on PSCs. This design can be further evolved by step-by-step modification and/or introducing other motifs.

Conclusion

We designed and synthesised D–π–D passivation molecules (PM) bearing hydrophilic n-dodecylphenyl and hydrophobic DEG-phenyl in a *C*$_2$-symmetric (*syn*-isomer) or *anti*-symmetric manner (*anti*-isomer). Owing to the HOMO energy levels being well aligned with PVK, PM-*syn* and PM-*anti* showed efficient hole transfer from PVK, as revealed by PL quenching, TRPL, and TRMC. Upon treatment with these PMs, the hydrophobicity of PVK increased, whereas its crystallite orientation remained unchanged. As a result, the PM-*syn*-treated PSC exhibited improved PCE (18.79%) and stability compared with the control (PCE = 17.98%). We also introduced a *C*$_3$-symmetric motif of TRX with carboxyl units as bifacial passivation molecules in PSCs. Notably, TRX-*syn*-treated PSC exhibited a higher PCE of 19.76% and better stability than the control and TRX-*anti*-based PSCs. Therefore, we foresee the possibility of a bifacial passivation molecule for PSC applications that can satisfy both the performance and stability requirements.

Experimental

General measurement
Steady-state photoabsorption and photoluminescence spectroscopy were performed using Jasco V-730 ultraviolet-visible (UV-Vis) and Jasco FP-8300 spectrophotometers, respectively. Fourier-transform infrared (FT-IR) spectroscopy was performed using a Jasco FT/IR-4700AC spectrometer. Photoelectron yield spectroscopy (PYS) was performed using a Bunko Keiki BIP-KV202GD instrument. X-ray diffraction (XRD) measurements were performed using Rigaku Corp. MiniFlex-600 instrument (Cu Kα radiation: *λ* = 1.54 Å). 2-dimensional grazing-incidence X-ray diffraction (2D-GIXRD) was performed on the BL13XU beamline at SPring-8 (Japan Synchrotron Radiation Research Institute, JASRI), using 12.39 keV (*λ* = 1 Å) X-rays and a grazing incidence angle of 0.12°. Two-dimensional (2D) diffraction patterns were recorded using a 2D detector (Dectris PILATUS 300 K). The thickness of each layer was measured by using a Bruker Dektak XT surface profiler. Scanning electron microscopy (SEM) was performed at 5 keV using a JEOL JSM-IT700HR instrument. ^{1}H NMR (400 MHz) and ^{13}C NMR (100 MHz) spectra were recorded using a JEOL JNM-ECZS400 spectrometer. High-resolution fast atom bombardment mass spectrometry (FAB-MS) was performed using a JEOL JMS-700 instrument. Recycling preparative chiral HPLC was performed using a LaboACE LC-7080 Plus recycling preparative HPLC system (Japan Analytical Industry), equipped with a CHIRAL ART Amylose-SA column (YMC Co., Ltd., diameter: 20 mm; length: 250 mm). Analytical chiral HPLC was performed at 25 °C on a JASCO PU-4180 equipped with a column CHIRAL ART Amylose-SA column, YMC Co., Ltd. (diameter: 4.6 mm; length: 250 mm) and a UV detector (UV-4075) at a flow rate of 0.40 mL min^{-1}. Chromatograms were recorded and analysed using JASCO ChromNAV Ver.2 software system. Time-resolved photoluminescence (TRPL) measurements based on a time-correlated single-photon counting (TCSPC) technique were performed on a HORIBA model FluoroCube 3000U-UltraFast-SP

Journal Name

spectrophotometre (λ_{ex} = 377 nm, resolution< 50 ps). The contact angle was measured using an Asumi Giken CAME1. Flash photolysis time-resolved microwave conductivity (TRMC) measurements were performed on the samples on a quartz plate. The excitation laser from an optical parametric oscillator (OPO, Continuum Inc., Panther) seeded by the third harmonic generation (355 nm) of a Nd:YAG laser (Continuum Inc., Surelite II, 5–8 ns pulse duration, 10 Hz) was set to 500 nm at I_0 = 1.3 × 10^{10} photons cm^{-2} pulse^{-1}. The laser pulse was exposed on the top side (not on the quartz side). The photoconductivity transient $\Delta\sigma$ was converted to the product of the quantum efficiency (φ) and the sum of the charge carrier mobilities, $\Sigma\mu$ (= $\mu_h + \mu_e$) by $\varphi\Sigma\mu = \Delta\sigma\,(eI_0F_{light})^{-1}$, where e and F_{light} are the unit charge of a single electron and a correction (or filling) factor, respectively. Dynamic light scattering (DLS) was performed using a Malvern PANalytical Zetasizer Lab (laser wavelength: 633 nm). All experiments were conducted at room temperature in air.

Perovskite solar cell fabrication

An FTO layer on a glass substrate was etched with 6-mol dm^{-3} HCl and Zn using a masking tape. After cleaning with detergent, acetone, isopropyl alcohol, and deionised water, a compact TiO$_2$ (cTiO$_2$) layer was deposited onto the FTO/glass by spray pyrolysis using a solution of titanium diisopropoxide bis(acetylacetonate) (Tokyo Chemical Industry Co. Ltd., TCI) in ethanol (1:14 v/v) at 450 °C. A 200-nm mesoporous TiO$_2$ (mpTiO$_2$) layer (average particle size: 30 nm, anatase) was deposited onto the compact TiO$_2$ layer by spin-coating (slope 3 s, 5,000 rpm for 15 s, slope 2 s) of a diluted TiO$_2$ paste (PST–30NR-D, GreatCell Solar Ltd.) in ethanol (paste:ethanol = 1:7 w/w), followed by sintering at 500 °C for 20 min. A 1.4 M N,N'-dimethylformamide (DMF, super dehydrated, Wako):dimethyl sulfoxide (DMSO, super dehydrated, Wako) = 4:1 (v/v%) solution of FAI ((NH$_2$)$_2$CHI), PbI$_2$, MABr (CH$_3$NH$_3$Br), and PbBr$_2$ with a 0.87:0.13 stoichiometry (the amount of FAI was reduced to FAI / PbI$_2$ = 0.95) was prepared in an N$_2$-filled glovebox. Solar cell grade perovskite precursors were purchased from TCI and used as received. Subsequently, a precursor layer was formed by spin coating the solution (slope = 1 s, 1,000 rpm = 10 s, slope = 4 s, 4500 rpm = 30 s, and slope = 2 s). After 35 s, poor-solvent treatment (chlorobenzene, anhydrous 99.8%, Sigma-Aldrich) was applied by slowly dropping 180 µL onto the rotating substrate. The resultant transparent film was annealed at 100 °C for 40 min, resulting in a 300-nm perovskite layer. The passivation layer was spun cast at 5000 rpm for 15 s from a super-anhydrous CB solution for PM or a super-anhydrous IPA solution for TRX (0.5–3 mg mL^{-1}; 3 mg mL^{-1} was optimal for PM and 0.5 mg mL^{-1} for TRX). A 50-nm layer of spiro-OMeTAD (Borun New Material Technology Ltd.) was deposited by spin-coating 78.2 mg mL^{-1} chlorobenzene (Sigma-Aldrich, anhydrous, 99.8%) with 52 mol% of LiTFSI (TCI, TFSI is bis(trifluoro methanesulfonyl)imide) relative to spiro-OMeTAD dissolved in acetonitrile (Sigma-Aldrich, anhydrous, 99.8%) and 2.9 vol% 4-*tert*-butylpyridine (TBP, Combi-Blocks, 98%) relative to the solution volume. Subsequently, a 70-nm stripe-shaped gold electrode was thermally deposited in a vacuum chamber. To promote oxygen doping of the HTL, the devices were stored

in an oxygen-substituted desiccator in the dark for three days. Current-voltage curves were measured using a source meter unit (ADCMT Corp., 6241A) under AM1.5G solar illumination at 100 mW cm^{-2} (1 sun, monitored by a calibrated standard cell, Bunko Keiki BS-520BK) from a 300-W solar simulator (SAN-EI Corp., XES-301S). The size of the active area was determined using a black metal mask with a square hole (2 × 2 mm^2). The external quantum efficiency (EQE) spectra were measured using a Bunko Keiki model SM-250KD equipped with a Keithley model 2401 source meter. The monochromated light power was calibrated using a silicon photovoltaic (PV) cell (Bunko Keiki model S1337-1010BQ). The devices used for stability tests were stored in an environmental test chamber (ESPEC Corp. SH-222) at 30 °C and a relative humidity (RH) of 60–65%.

Conflicts of Interest

The authors declare no competing financial interests.

References

1   F. Li, F. R. Lin and A. K.-Y. Jen, *Adv. Mater.*, 2024, **36**, 2307161.
2   H.-S. Kim and N.-G. Park, *Adv. Energy Mater.*, 2024, **13**, 2400089.
3   P. Zhu, C. Chen, J. Dai, Y. Zhang, R. Mao, S. Chen, J. Huang and J. Zhu, *Adv. Mater.*, 2024, **36**, 2307357.
4   A. Kojima, K. Teshima, Y. Shirai and T. Miyasaka, *J. Am. Chem. Soc.* , 2009, **131**, 6050– 6051.
5   H.-S. Kim, C.-R. Lee, J.-H. Im, K.- B. Lee, T. Moehl, A. Marchioro, J. S. Moon, R. Humphry-Baker, J.- H. Yum, J. E. Moser, M. Grätzel and N.–G. Park, *Sci. Rep.*, 2012, **2**, 591.
6   M. M. Lee, J. Teuscher, T. Miyasaka, T. N. Murakami and H. J. Snaith, *Science* , 2012, **338**, 643–647.
7   J. S. Manser, Christians. J. A. and P. V. Kamat, *Chem. Rev.*, 2016, **116**, 12956–13008.
8   A. Miyata, A. Mitioglu, P. Plochocka, O. Portugall, J. T.-W. Wang, S. D. Stranks, H. J. Snaith and R. J. Nicholas, *Nat. Phys.*, 2015, **11**, 582–587.
9   S. D. Stranks, G. E. Eperon, G. Grancini, C. Menelaou, M. J. P. Alcocer, T. Leijtens, L. M. Herz, A. Petrozza and H. J. Snaith, *Science*, 2013, **342**, 341–344.

10   D. A. Valverde-Chavez, C. S.Jr. Ponseca, C. C. Stoumpos, A. Yartsev, M. G. Kanatzidis, V. Sundstorm and D. G. Cooke, *Energy Environ. Sci.*, 2015, **8**, 3700–3707.

11   H. Oga, A. Saeki, Y. Ogomi, S. Hayase and S. Seki, *J. Am. Chem. Soc.*, 2014, **136**, 13818–13825.

12   Y. Zhao, F. Ma, Z. Qu, S. Yu, T. Shen, H.-X. Deng, X. Chu, X. Peng, Y. Yuan, X. Zhang and J. You, *Science*, 2022, **377**, 531–534.

13   J. Park, J. Kim, H.-S. Yun, M. J. Paik, E. Noh, H. J. Mun, M. G. Kim, T. J. Shin and S. I. Seok, *Nature*, 2023, **616**, 724–730.

14   M. K. Rao, D. N. Sangeetha, M. Selvakumar, Y. N. Sudhalker and M. G. Mahesha, *Solar Energy*, 2021, **218**, 469–491.

15   Y. An, J. Hidalgo, C. A. R. Perini, A. F. Castro-Méndez, J. N. Vagott, K. Bairley, S. Wang, X. Li and J.-P. Correa-Baena, *ACS Energy Lett.*, 2021, **6**, 1942–1969.

16   L. D. Marco, G. Nasti, A. Abate and A. Rizzo, *Sol. RRL*, 2022, **6**, 2101085.

17   R. Shimono, R. Nishikubo, F. Ishiwari and A. Saeki, *J. Phys. Chem. C.*, 2022, **126**, 17894–17903.

18   Y. Jiang, J. Wang, H. Zai, D. Ni, J. Wang, P. Xue, N. Li, B. Jia, H. Lu, Y. Zhang, F. Wang, Z. Guo, Z. Bi, H. Xie, Q. Wang, W. Ma, Y. Tu, H. Zhou and X. Zhan, *J. Am. Chem. Soc.*, 2022, **144**, 5400–5410.

19   B. Wang, H. Wang, G. Sathiyan, C. Chen, Y. Xu and M. Cheng, *ACS Appl. Energy Mater.*, 2022, **5**, 5901–5908.

20   R. E. Brandt, J. R.: GoraiP. Poindexter, R. C. Kurchin, R. L. Nienhaus, M. W. B. Wilson, J. A. Polizzotti, R. Sereika, R. Zaltauskas, L. C. Lee, J. L. MacManus-Driscoll, M. Bawendi, V. Stevanovic and T. Buonassisi, *Chem. Mater.*, 2017, **29**, 4667–4674.

21   A. R. bin M. Yusoff, M. Vasilopoulou, D. G. Georgiadou, L. C. Palilis, A. Abate and M. K. Nazeeruddin, *Energy Environ. Sci.*, 2021, **14**, 2906–2953.

22   J. Chen and N.-G. Park, *ACS Energy Lett.*, 2020, **5**, 2742–2786.

23   D. Zhang, D. Li, Y. Hu, A. Mei and H. Han, *Commun. Mater.*, 2022, **3**, 58.

24   Q. Jiang, Y. Zhao, X. Zhang, X. Yang, Y. Chen, Z. Chu, Q. Ye, X. Li, Z. Yin and J. You, *Nat. Photonics*, 2019, **13**, 460–466.

25   Q. Wang, X. Zheng, Y. Deng, J. Zhao, Z. Chen and J. Huang, *Joule*, 2017, **1**, 371–382.

26   M. Abdi-Jalebi, Z. Andaji-Garmaroudi, S. Cacovich, C. Stavrakas, B. Philippe, J. M. Richter, M. Alsari, E. P. Booker, E. M. Hutter, A. J. Pearson, S. Lilliu, T. J. Savenije, H. Rensmo, G. Divitini, C. Ducati, R. H. Friend and S. D. Stranks, *Nature*, 2018, **555**, 497–501.

27   N. K. Noel, A. Abate, S. D. Stranks, E. S. Parrott, V. M. Burlakov, A. Goriely and H. J. Snaith, *ACS Nano*, 2014, **8**, 9815–9821.

28   T. Li, Y. Zhang, L. Fang, B. Zhang, Y. Yuan, J. Zhang and P. Wang, *J. Mater. Chem. A.*, 2023, **11**, 15269–15276.

29   T. Wu, X. Li, Y. Qi, Y. Zhang and L. Han, *ChemSusChem*, 2021, **14**, 4354–4376.

30   M. Guo, J. Xu, J. Li, J. Huang, J. Zhu, Y. Li, P. Gao, J. Li and M. Wei, *J. Mater. Chem. A.*, 2023, **11**, 8299–8307.

31   X. Li, C.-C. Chen, M. Cai, X. Hua, F. Xie, X. Liu, J. Hua, Y.-T. Long, H. Tian and L. Han, *Adv. Energy Mater.*, 2018, **8**, 1800715–1800721.

32   A. A. Sutanto, C. Igci, H. Kim, H. Kanda, N. Shibayama, M. Mensi, V. I. E. Queloz, C. Momblona, H. J. Yun, H. J. Bolink, A. J. Huckaba, Yun and M. K. Nazeeruddim, *ACS Appl. Energy Mater.*, 2021, **4**, 1259–1268.

33   Y.-D. Wang, Y. Wang, J.-Y. LanY. Shao, Z.-R. Lan, Y.-W. Zhong and Y. Song, *ACS Energy Lett.*, 2021, **6**, 2030–2037.

34   Q. Yang, X. Liu, S. Yu, Z. Feng, L. Liang, W. Qin, Y. Wang, X. Hu, S. Chen, Z. Feng, G. Hou, K. Wu, X. Guo and C. Li, *Energy Environ. Sci.*, 2021, **14**, 6536–6545.

35   T. Wu, R. Zhao, J. Qiu, S. Wang, X. Zhang and Y. Hua, *Adv. Funct. Mater.*, 2022, **37**, 2204450.

36   N. Minoi, F. Ishiwari, K. Murotani, R. Nishikubo, T. Fukushima and A. Saeki, *ACS Appl. Mater. Interfaces*, 2023, **15**, 6708–6715.

37   B. Chen, P. N. Rudd, S. Yang, Y. Yuan and J. Huang, *Chem. Soc. Rev.*, 2019, **48**, 3842–3867.

38   T. Fukui, K. Hofuku, A. Kosaka, N. Minoi, R. Nishikubo, F. Ishiwari, H. Sato, A. Saeki and T. Fukushima, *Small Struct.*, 2024, **5**, 230041.

39   R. Dorel and A. M. Echavarren, *Acc. Chem. Res.*, 2019, **52**, 1812–1823.

40   T. Omine, F. Ishiwari, T. Won, N. Aizawa, Y. Takeda, Y. Yakiyama, T. Mori, T. Hirose, K.-i. Nakayama and A. Saeki, *ChemRxiv,* DOI:10.26434/chemrxiv-2024-m8drx.

41   S. Yang, J. Dai, Z. Yu, Y. Shao, Y. Zhou, X. Xiao, X. C. Zeng and J. Huang, *J. Am. Chem. Soc.*, 2019, **141**, 5781–5787.

42   C. Huang, W. Fu, C.-Z. Li, Z. Zhang, W. Qiu, M. Shi, P. Heremans, A. K.-Y. Jen and H. Chen, *J. Am. Chem. Soc.*, 2016, **138**, 2528–2531.

43   R. Ramanujam, H.-L Hsu, Z.-E. Shi, C.-Y. Lung, C.-H. Lee, G. Z. Wubie, C.-P. Chen and S. S. Sun, *Small*, 2024, **20**, 2310939.

44   E. Aktas, J. Jiménez-López, C. Rodríguez-Seco, R. Pudi, M. A. Ortuño, N. López and E. Palomares, *ChemPhysChem*, 2019, **20**, 2702– 2711.

45   M. A. Truong, Funasaki T., L. Ueberricke, W. Nojo, R. Murdey, T. Yamada, S. Hu, A. Akatsuka, N. Sekiguchi, S. Hira, L. Xie, T. Nakamura, N. Shioya, D. Kan, Y. Tsuji, S. Iikubo, H. Yoshida, Y. Shimakawa, T. Hasegawa, Y. Kanemitsu, T. Suzuki and A. Wakamiya, *J. Am. Chem. Soc.*, 2023, **145**, 7528–7539.

46   D. Baunsgaard, N. Harrit, F. Negri, G. Orlandi, J. Frederiksen and R. Wilbrandt, *J. Phys. Chem. A*, 1998, **102**, 10007–10016.

47   S. J. Sung, J. Im, G. Kim, C. S. Moon, J. J. Yoo, S. S. Shin, N. J. Jeon, B. S. Ma, D. J. Kim, T.-S. Kim and J. Seo, *Adv. Energy Mater.*, 2022, **12**, 2200758.

48   Y. Murakami, R. Nishikubo, F. Ishiwari, K. Okamoto, T. Kozawa and A. Saeki, *Mater. Adv.*, 2022, **3**, 4861–4869.

49   A. Saeki, *Polym. J.*, 2020, **52**, 1307–1321.

50   N. Ishida, A. Wakamiya and A. Saeki, *ACS Photonics*, 2016, **3**, 1678–1688.

51   E. M. Hutter, J.-J. Hofman, M. L. Petrus, M. Moes, R. D. Abellón, P. Docampo and T. J. Savenije, *Adv. Energy Mater.*, 2017, **7**, 1602349.

52   L. Krückemeier, Z. Liu, T. Kirchartz and U. Rau, *Adv. Mater.*, 2023, **35**, 2300872.

53   M. T. Weller, O. J. Weber, J. M. Frost and A. Walsh, *J. Phys. Chem. Lett.*, 2015, **6**, 3209–3212.

54   J. B. Patel, Q. Lin, O. Zadvorna, C. L. Davies, L. M. Herz and M. B. Johnston, *J. Phys. Chem. Lett.*, 2018, **9**, 263–268.

55   Q. Jiang, Y. Zhao, X. Zhang, X. Yang, Y. Chen, Z. Chu, Q. Ye, X. Li, Z. Yin and J. You, *Nat. Photo.* 2019, **13**, 460–466.

56   L. Zhao, Q. Li, C.-H. Hou, S. Li, X. Yang, J. Wu, S. Zhang, Q. Hu, Y. Wang, Y. Zhang, Y. Jiang, S. Jia, J.-J. Shyue, T. P. Russell, Q. Gong; X. Hu and R. Zhu, *J. Am. Chem. Soc.* 2022, **144**, 1700–1708.

57   J. Wang, K. Wang, C. Zhang, S. Liu, X. Guan, C. Liang, C.-C. Chen and F. Xie, *Adv. Energy Mater.* 2023, **13**, 2302169–2302178.

The data supporting this article have been included as part of the Supplementary Information.